

NOTES AND CORRESPONDENCE

Resonant Forcing of Mixed Layer Inertial Motions by Atmospheric Easterly Waves in the Northeast Tropical Pacific*

JOHN B. MICKETT

Applied Physics Laboratory, University of Washington, Seattle, Washington

YOLANDE L. SERRA

Institute for Atmospheric Physics, The University of Arizona, Tucson, Arizona

MEGHAN F. CRONIN

NOAA/Pacific Marine Environmental Laboratory, Seattle, Washington

MATTHEW H. ALFORD

Applied Physics Laboratory, and School of Oceanography, University of Washington, Seattle, Washington

(Manuscript received 28 April 2009, in final form 6 August 2009)

ABSTRACT

Westward-propagating atmospheric easterly waves contribute to much of the variability of the low-level wind fields within the northeast tropical Pacific. With the dominant period of these waves (3–5 days) close to the local inertial period (2.4 days at 12°N to 5.7 days at 5°N), there is the expectation that the associated winds may resonantly force mixed layer inertial motions in this region. The authors test this hypothesis using a simple slab model and roughly 4½ yr of wind data from four NOAA Tropical Atmosphere Ocean/Eastern Pacific Investigation of Climate Processes (TAO/EPIC) buoys along 95°W at 12°, 10°, 8°, and 5°N. The degree of resonance is determined by comparing model simulations using observed wind stress with simulations forced with reversed-rotation wind stress. Results strongly indicate that Pacific easterly waves (PEWs) resonantly force inertial motions in the region. This resonance shows both significant seasonality and latitudinal dependence that appears to be related to the meridional position and intensity of the PEWs. North of the zonal axis of the mean track of the PEWs, the low-level winds associated with the waves rotate predominantly clockwise with time and resonantly force mixed layer inertial motions. South of this axis, the winds rotate counterclockwise, resulting in dissonant (antiresonant) forcing. As this axis migrates annually from about 4°N during the boreal winter/spring to a maximum northerly position of about 8°–10°N in the late boreal summer/early fall, the region of strongest resonance follows, consistently remaining to its north. Model output suggests that resonant forcing results in roughly 10%–25% greater net annual flux of kinetic energy from the wind to mixed layer inertial motions than in neutral or nonresonant conditions. This finding has strong implications for mixed layer properties, air–sea coupling, and the generation of near-inertial internal waves.

* Pacific Marine Environmental Laboratory Contribution Number 3299.

Corresponding author address: J. B. Mickett, Applied Physics Laboratory, University of Washington, 1013 NE 40th St., Seattle, WA 98105.
E-mail: jmickett@apl.washington.edu

1. Introduction

Weakly damped systems have the potential to become resonant when the forcing is closely tuned to the preferential or natural frequency response of the system. In the case of the ocean mixed layer, which has a dominant response to wind stress in the form of inertial motions with frequencies near the local Coriolis frequency f ,

resonance is likely to occur when the wind stress vector (τ) either rotates in phase with the mixed layer inertial motions or forces the mixed layer in pulses so that τ is aligned with the rotating mixed layer currents. In their seminal work on the wind generation of mixed layer inertial motions, Pollard and Millard (1970, hereafter PM70) recognized the potential for inertially rotating wind stress to resonantly force the mixed layer.

Forcing the simple mixed layer slab model introduced in PM70 with wind stress associated with a variety of storm events, D'Asaro (1985) found that at midlatitudes resonance is important to the flux of kinetic energy from the wind to the mixed layer. Smaller, faster-moving fronts and storms with time scales of close to $1/f$ are found to more effectively force inertial motions than larger, slower-moving storms with time scales much greater than $1/f$. In the latter case, inertial motions generated during the early stages of the large, slow synoptic-scale features are subsequently arrested in the later stages. Of the small [$O(100 \text{ km})$], fast-moving features, cold fronts are specifically shown to resonantly force inertial motions, with winds rotating clockwise (in the Northern Hemisphere) with time at a frequency close to f .

Crawford and Large (1996) investigated potential impacts of resonant wind forcing with the one-dimensional (1D) K -profile parameterization (KPP; Large et al. 1994) numerical model, finding that it maximizes the atmospheric input of kinetic energy (KE) to mixed layer currents as well as the net changes in mixed layer inertial kinetic energy (IKE) and total potential energy (PE). Investigating resonant wind forcing using a large eddy simulation (LES) model, Skillingstad et al. (2000) obtain similar results showing that resonance produces the largest mixed layer velocities and vertical mixing. Both Crawford (1993) and Large and Crawford (1995) show that storms with the largest inertial currents also produce the most dramatic changes in SST, suggesting that resonant forcing may influence air–sea coupling. With much of the mixed layer wind-forced IKE eventually propagating into the thermocline as near-inertial internal waves (e.g., D'Asaro et al. 1995; Crawford and Large 1996), the intensity and geographic distribution of resonant forcing also has implications for deep mixing and the maintenance of abyssal stratification (e.g., Alford 2001; Watanabe and Hibiya 2002; Alford 2003).

Here we investigate the potential for resonant mixed layer forcing in the northeast tropical Pacific (Fig. 1). In this region, outgoing longwave radiation (OLR) and low-level wind fields in the intertropical convergence zone (ITCZ) are strongly influenced by convectively coupled propagating waves on synoptic time scales (e.g., Tai and Ogura 1987; Lau and Lau 1990; Gu and Zhang 2002; Roundy and Frank 2004; Serra et al. 2008),

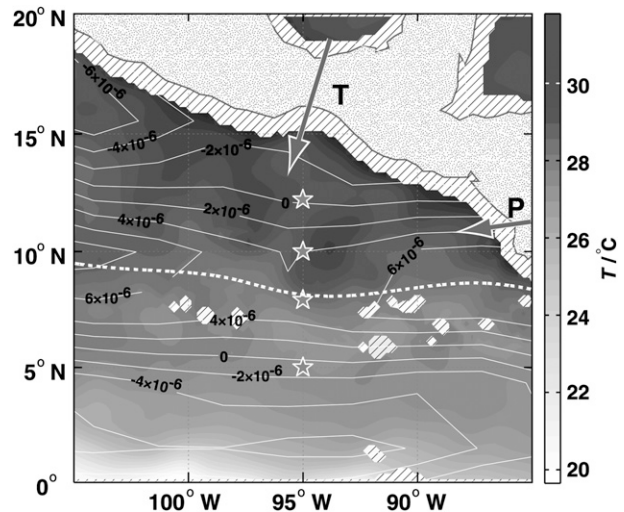


FIG. 1. Map of the study area with stars indicating the locations of the four TAO/EPIC buoys used for this study, nominally at 12°, 10°, 8°, and 5°N along the 95°W line. White contours are ERA-interim 600-hPa T42 smoothed vorticity climatology for July–September for 1999–2003, showing the mean PEW track for this period as a zonal swath of maximum vorticity. The latitude of maximum vorticity (dashed white line), roughly representing the zonal axis of the PEWs, is calculated after cubic interpolation of vorticity onto a finer grid. Filled contours show 4-day-averaged (12 Sep–1 Jan 2001), 2° smoothed SST as measured by the Tropical Rainfall Measuring Mission (TRMM) satellite, with data gaps indicated with hatching. Arrows show locations of the Tehuantepec (T) and Papagayo (P) mountain gap wind jets.

with the dominant synoptic atmospheric disturbances westward-propagating Pacific easterly waves (PEWs; Chang 1970; Reed and Recker 1971; Nitta et al. 1985; Tai and Ogura 1987; Lau and Lau 1990; Gu and Zhang 2002; Serra and Houze 2002; Petersen et al. 2003; Serra et al. 2008). PEWs in the northeast tropical Pacific have periods of roughly 3–5 days, wavelengths of about 4400 km, and westward phase speeds of about 11 m s^{-1} (e.g., Serra and Houze 2002; Petersen et al. 2003; Serra et al. 2008). With the period of PEWs similar to the local inertial period at these latitudes ($2\pi/f = 2.4$ days at 12°N to 5.7 days at 5°N), wind stress associated with PEWs has the potential to resonantly force mixed layer motions. Thus, unlike the findings of D'Asaro (1985) showing that midlatitude synoptic-scale features contain little energy at near-inertial frequencies, at low-latitudes there is considerable overlap between the dominant frequencies of atmospheric forcing and the preferred frequency response of the mixed layer. Additionally, with the amplitude of slablike mixed layer currents resulting from wind stress approximately proportional to the inverse of the mixed layer depth (e.g., Pollard and Millard 1970), an exceptionally shallow mixed layer throughout much of this region ($<30 \text{ m}$)

indicates that the northeast tropical Pacific may be particularly sensitive to resonant forcing.

Using the simple PM70 slab model and roughly 4½ yr of wind data from four National Oceanic and Atmospheric Administration (NOAA) Tropical Atmosphere Ocean/Eastern Pacific Investigation of Climate Processes (TAO/EPIC) buoys along 95°W at 12°, 10°, 8°, and 5°N, we show evidence that PEWs resonantly force inertial motions within the northeast tropical Pacific. At three of the locations (8°, 10°, and 12°N), resonant wind forcing—much of which appears to be associated with PEWs—results in about 10%–25% greater net annual flux of IKE from the wind to the mixed layer than would result from neutral or nonresonant conditions. At 5°N, where resonant forcing is observed during the winter but dissonance is observed from roughly April to November, model results show resonance has a small net annual effect, with counterclockwise (CCW) rotation of winds potentially acting to reduce the net annual IKE flux.

The general pattern of resonant forcing at the study locations shows both significant seasonality and latitudinal dependence that appears to be largely related to the meridional position and intensity of PEWs. PEWs are most active from June to November (Roundy and Frank 2004; Serra et al. 2008) and are precursors to a majority of tropical eastern Pacific hurricanes (Avila 1991; Avila and Guiney 1998). The June–November mean wave axis crosses Central America near Panama and remains at approximately 5°–10°N into the central and east Pacific, whereas smaller vortices travel along the west coast of Mexico and Central America in association with strong convective activity (Serra et al. 2008). Similar vortices have been observed by Wang and Magnusdottir (2006) and are thought to be related to breakdown of the ITCZ associated with easterly waves and tropical disturbances interacting with the Sierra Madre and the mean ITCZ flow in this region. Surface wind patterns associated with both the main PEW axis as well as those along the coast are of interest to this study.

Viewing the horizontal structure of low-level winds associated with PEWs as alternating cyclonic and anticyclonic circulation cells arranged roughly zonally (Fig. 2a), as the wave propagates westward passing a fixed point, the local wind will complete one revolution over the period of the PEWs. One would expect CW wind rotation with time and thus potential resonant forcing north of the largely zonal axis of the PEWs and CCW rotation with time and potential dissonant forcing south of this axis (Fig. 2b). The strongest wind stress and resonance is expected to be associated with the passage of the cyclonic tropical depression (TD) phase of PEWs. With the PEW axis collocated with the ITCZ, as the ITCZ migrates meridionally with the

seasons from about 4°N in the boreal winter/spring to its most northerly position of about 8°–10°N in late boreal summer/early fall (Gruber 1972; Mitchell and Wallace 1992), the region of expected resonance should also migrate meridionally, remaining to the north of the ITCZ axis.

2. Methods

a. Data

Data used in this study are from four NOAA TAO/EPIC buoys positioned along 95°W at 5°, 8°, 10°, and 12°N (Fig. 1). Observations span May 1999 through October 2003, a period of enhanced air–sea flux and upper ocean monitoring (Cronin et al. 2002, 2006). Near-surface (4 m) wind speed and direction were measured using an R. M. Young propeller/vane anemometer and were sampled at 2 Hz over a 2-min sampling period with data recorded every 10 min. After extrapolating 4-m winds to 10 m assuming a log layer (with z_0 based on near-surface wind profiles at 10°N, 95°W), wind data are used to compute surface momentum flux (wind stress) using the Large and Pond (1981) bulk algorithm. Wind stress is used to both investigate the spectral characteristics of the wind forcing and to force the PM70 slab model.

Upper ocean temperature, which is used to estimate the mixed layer depth H , was sampled and recorded once every 10 min using YSI thermistors, with data used here from 5, 10, 20, 40, and 60 m. Specifically, H is defined as the shallowest depth at which $[T(5) - T(z)] > 0.17^\circ\text{C}$ using daily averaged values of T . Temperature data from a depth of 1 m were intentionally excluded from this definition to avoid the influence of short-lived, near-surface temperature stratification and because of numerous data gaps in the 1-m data. Because of the sharpness of the thermocline in the study region, the estimated value for H is rather insensitive to the threshold value used, with the specific value chosen because it minimizes the difference of observed and modeled mixed layer inertial current amplitudes over a wide range of model decay parameters. Physically, H is intended to represent the upper layer of the ocean over which vertical momentum fluxes are large and, consequently, over which velocities are relatively uniform with depth. Mixed layer velocity data, which are used to validate the model results, are from a Sontek single-point acoustic current meter (ACM) at 10-m depth with 10-min data averaged to 20 min. Temporal coverage of wind and thermistor measurements is relatively good, spanning more than 90% of the roughly 4½-yr period for all buoys. Current meter data, however, has large gaps and spans from 5% of the study period at 10°N to 30% at 8°N.

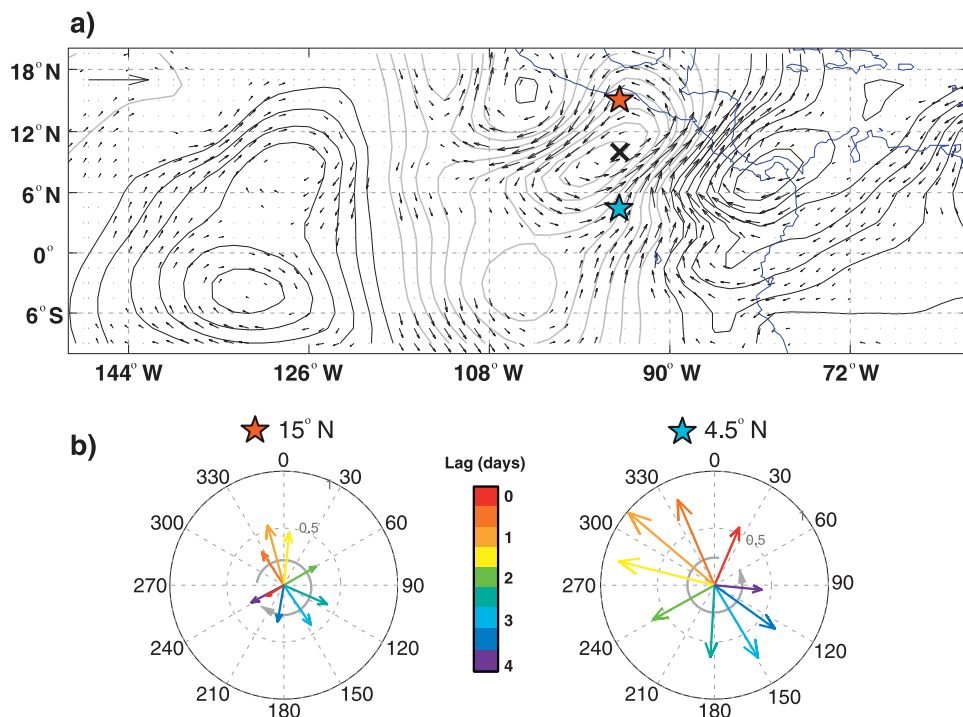


FIG. 2. (a) The 40-yr European Centre for Medium-Range Weather Forecasts (ECMWF) Re-Analysis interim 700-hPa winds and streamfunction regressed onto TD-filtered OLR at 10°N , 95°W (black X) for the June–November 1989–1998 time periods. The reference arrow on the top left is 1 m s^{-1} . (b) Compass plots of regressed 700-hPa winds at (left) 15°N and (right) 4.5°N , with vector length showing wind magnitude and color showing lag (0–4 days). The OLR filter selects westward planetary wavenumbers 6–20 and periods of roughly 2–6 days, corresponding to the easterly wave peak in the OLR space–time spectrum (Wheeler and Kiladis 1999). Using a -20 m^{-2} OLR anomaly at the base point (X), the regressions highlight the structure of PEWs in the east Pacific.

b. The slab model

1) MODEL FORMULATION

The PM70 model is a simple linear analytical solution describing the response of a depth-uniform (slab) mixed layer given a prescribed time-varying surface momentum flux $\tau(t)$ and mixed layer depth $H(t)$.¹ This particular model is appealing to use for this study because both input variables can be easily estimated from TAO/EPIC mooring measurements. Unlike 1D models that output H [e.g., PWP (Price et al. 1986) and KPP (Large et al. 1994)], the prescribed mixed layer depth avoids the need to reinitialize model runs when there are excessive departures of H from observations. The model assumes an f plane, vertically and horizontally uniform density ρ and velocity \mathbf{u} within the mixed layer and that the surface momentum flux acts as a body force over the mixed layer. Because the model assumes both vertical and horizontal

homogeneity, the modeled velocities are ageostrophic, partitioned into an inertial \mathbf{u}_I and an Ekman \mathbf{u}_E response. The 1D assumption also neglects the potential influence of remotely generated, laterally propagating internal waves (or baroclinic Poincaré waves) with near-inertial frequencies, which may contribute to local mixed layer velocities in addition to local wind stress forcing. Although Plueddemann and Farrar (2006, hereafter PF06) found evidence that remote forcing is likely important farther west in the Pacific at 10°N , 125°W , as will be shown, the relatively good comparison of modeled and observed mixed layer near-inertial velocities in this study suggests that mixed layer inertial motions are largely locally forced.

The model employs artificial linear Rayleigh damping r that is intended to account for a variety of mixed layer momentum sinks, including that transferred to the thermocline by turbulent mixing and the radiation of internal waves. This decay term takes the form of an exponential in the solution for inertial oscillations, giving an e -folding time of mixed layer velocity of $1/r$. Expressed using complex notation as in D’Asaro (1985), the model is simply

¹ For a more comprehensive discussion of the PM70 model, see D’Asaro (1985) and PF06.

TABLE 1. Model damping coefficients r .

Location	$1/r$ (days)	r^2/f^2
12°N, 95°W	2.5	0.0234
10°N, 95°W	2.5	0.0336
8°N, 95°W	3	0.0363
5°N, 95°W	3.5	0.0681

$$\frac{\partial Z}{\partial t} + \omega Z = \frac{T}{H}, \quad (1)$$

where

$$Z = u + iv, \quad T = \frac{\tau_x + i\tau_y}{\rho}, \quad \text{and} \quad \omega = r + if.$$

D'Asaro (1985) notes that realistic model simulations require $r^2 \ll f^2$. Here, r is specifically chosen by minimizing the difference in autocorrelation sequences of buoy-measured (10-m depth) and modeled mixed layer velocities over lags of 0–7 days (as done by Alford 2001), with values used falling within the typical ocean parameter range of $1/r = 2$ –10 days (e.g., D'Asaro 1985; PF06; Table 1).

For this investigation, the model quantity of principal interest is the flux of IKE from the wind to the mixed layer Π_w , which is one of the primary energy pathways between the atmosphere and the ocean. Again, following D'Asaro (1985), decomposing the mixed layer velocities into the inertial and Ekman components (i.e., $Z = Z_I + Z_E$), the flux of inertial kinetic energy from the wind to the mixed layer in units of watts per meter squared is given by

$$\Pi_w = -\rho H \Re \left[\frac{Z_I^*}{\omega} \frac{d}{dt} \left(\frac{T}{H} \right) \right], \quad (2)$$

where Z_I^* is the complex conjugate of Z_I and positive values indicate energy transfer to the mixed layer. Fluxes of IKE from the wind to the mixed layer are driven by time changes of the vector quantity T/H but are dependent on the phase (direction) of the mixed layer inertial currents Z_I with respect to this vector. With wind stress typically much more variable than mixed layer depth, the flux of IKE is dominated by changes in T .

For heuristic purposes, it is helpful to consider a greatly simplified approximation of Eq. (2) that is the dot product of the wind stress vector and the mixed layer inertial velocities $\boldsymbol{\tau} \cdot \mathbf{u}_I$ or in complex form $\rho Z_I T^*$ (e.g., Alford 2001; PF06). Thus, generally wind stress in the direction of existing mixed layer inertial motions \mathbf{u}_I adds IKE to the mixed layer and that opposing \mathbf{u}_I removes IKE. Energy loss associated with negative Π_w is thought to be carried out largely through mixed layer turbulent dissipation, with turbulence accomplishing little work, because it “mixes” already well-mixed water. Additionally, because model velocity Z is solely driven by wind stress,

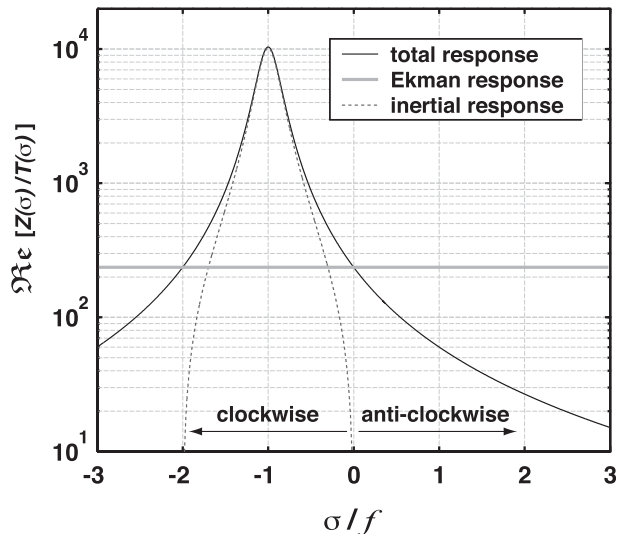


FIG. 3. PM70 model response function for mixed layer velocity using $H = 25$ m, $1/r = 3$ days, and a latitude of 10°N. Positive values of σ/f correspond to CCW rotation, and negative values correspond to CW rotation. Note the large peak at the (CW) inertial frequency, $\sigma/f = -1$, in both the total response (black) and inertial response (dashed gray). If the inertial component is out of phase with the Ekman component (solid gray), the total response will be less than the Ekman.

cumulative or time-integrated KE fluxes (i.e., wind work) must be positive and greater than the cumulative energy lost through damping, or no more energy than enters the system can be removed. For all calculations made here, the exact form of Π_w given by Eq. (2) is used.

Because Π_w is a function of the mixed layer inertial velocity that has a highly tuned inertial response (Fig. 3), there is the potential for Π_w to be sensitive to CW forcing close to f . However, as is illustrated in Fig. 4, the respective phases (direction) of these vectors are important for resonance to occur. Here, contours of model IKE flux are plotted versus the frequency of a constant-magnitude wind stress (x axis) and the normalized phase offset ($\Delta\phi/\Pi$) between the initial wind stress vector $\boldsymbol{\tau}(t=0)$ and a preexisting mixed layer inertial current $\mathbf{u}_I(t=0)$ of 0.3 m s^{-1} to the east (y axis). The IKE flux shown is computed using the full IKE flux equation [Eq. (2)] and is the average over the first inertial period. As expected, there is strong asymmetry in IKE flux between CW and CCW rotation of winds, with the largest values associated with CW rotation near the local Coriolis frequency.²

However, it is clear that phase of the wind stress with respect to existing inertial currents is also important, with negative IKE fluxes at f when the phase offset is

² The strongest fluxes occur when CW forcing is slightly super-inertial, which is a consequence of only averaging over the first inertial period.

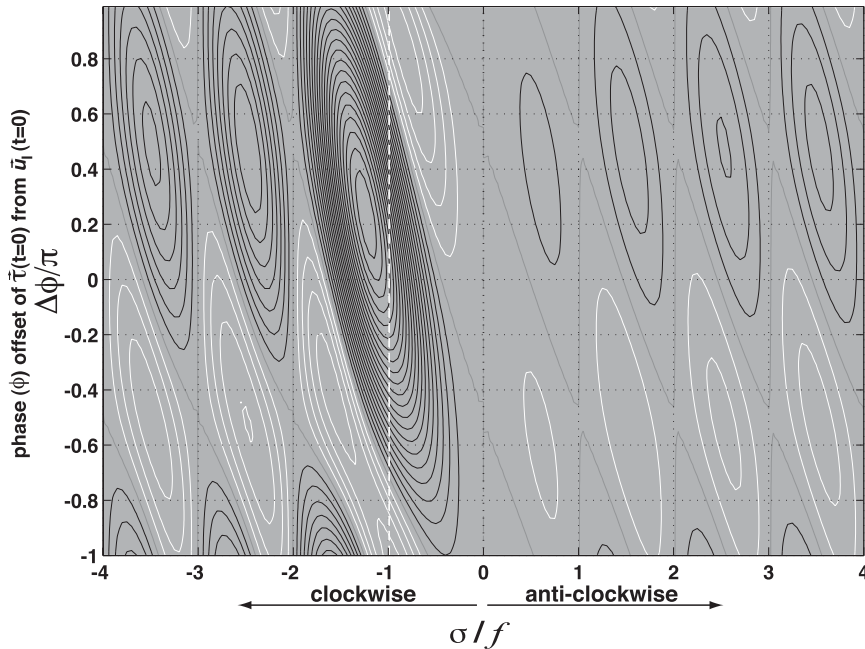


FIG. 4. Contours of IKE flux from the PM70 model plotted against normalized frequency σ/f of wind stress (x axis) and normalized phase offset $\Delta\phi/\pi$ between wind stress direction at time zero and a preexisting inertial current of 0.3 m s^{-1} to the east (y axis). The IKE flux shown is the average over one inertial period starting at time zero. Model settings are $H = 25 \text{ m}$, $r = 1/3$ days, a constant wind magnitude of 5 m s^{-1} , and a latitude of 10°N . The contour interval is 1 mW m^{-2} , with positive contours in black, negative contours in white, and the zero contour in gray. The inertial frequency is indicated with a dashed white line.

near $\pm\pi$. For CW rotation at f , positive fluxes occur over a greater range of phase offsets than negative fluxes do, whereas for CCW wind rotation this asymmetry is much weaker. If IKE flux is averaged over two inertial periods (versus one), we would find that the flux is positive at f for all phase offsets. This is a manifestation of the inertial velocity response function (Fig. 3), with CW rotation at f very effective at modifying existing mixed layer currents, realigning them so that the phases of $\boldsymbol{\tau}$ and \mathbf{u}_I become more coherent, with IKE fluxes consequently becoming positive. Also a consequence of this preferential response, at certain phase offsets and frequencies, CW rotation of wind can also more effectively remove IKE from the mixed layer (i.e., larger negative contours on the CW side of Fig. 4). In general, for systems with a response time that is short with respect to the natural period (as is the case here), there is a tendency for forcing at the natural frequency to rapidly reduce phase differences with the response. As will be shown in section 3b, this characteristic of resonant forcing is apparent in PEW-forced resonance.

2) THE TEST FOR RESONANCE

The degree of resonant forcing is estimated by comparing the wind-driven IKE flux from two different model simulations: a control simulation forced with the

observed wind stress Π_w and a test simulation using wind stress calculated with the rotation direction of the wind stress reversed but magnitude preserved Π_{wr} . Expressing the wind stress in complex form (i.e., $\boldsymbol{\tau} = \tau_x + i\tau_y$), reversed-rotation wind stress is obtained simply by changing the sign of one of the terms, or $\boldsymbol{\tau}_r = \tau_x - i\tau_y$. The difference in the IKE flux of the two simulations isolates the role of wind rotation, with resonance occurring when the observed wind stress (control) simulation results in greater wind stress-driven IKE flux than the reversed-rotation wind stress simulation. The opposite case suggests dissonant or antiresonant forcing, with wind stress often acting to remove energy from any existing inertial motions. To more clearly isolate the role of rotation, we choose to reverse the direction of the true wind stress rotation instead of simply generating a wind stress time series with no rotation (magnitude only).

Mathematically, the influence of wind stress rotation on Π_w is given by

$$\Pi_{w\phi} = \frac{\Pi_w - \Pi_{wr}}{2}, \quad (3)$$

where division by 2 is necessary because we want to compare observations to neutral conditions, or conditions

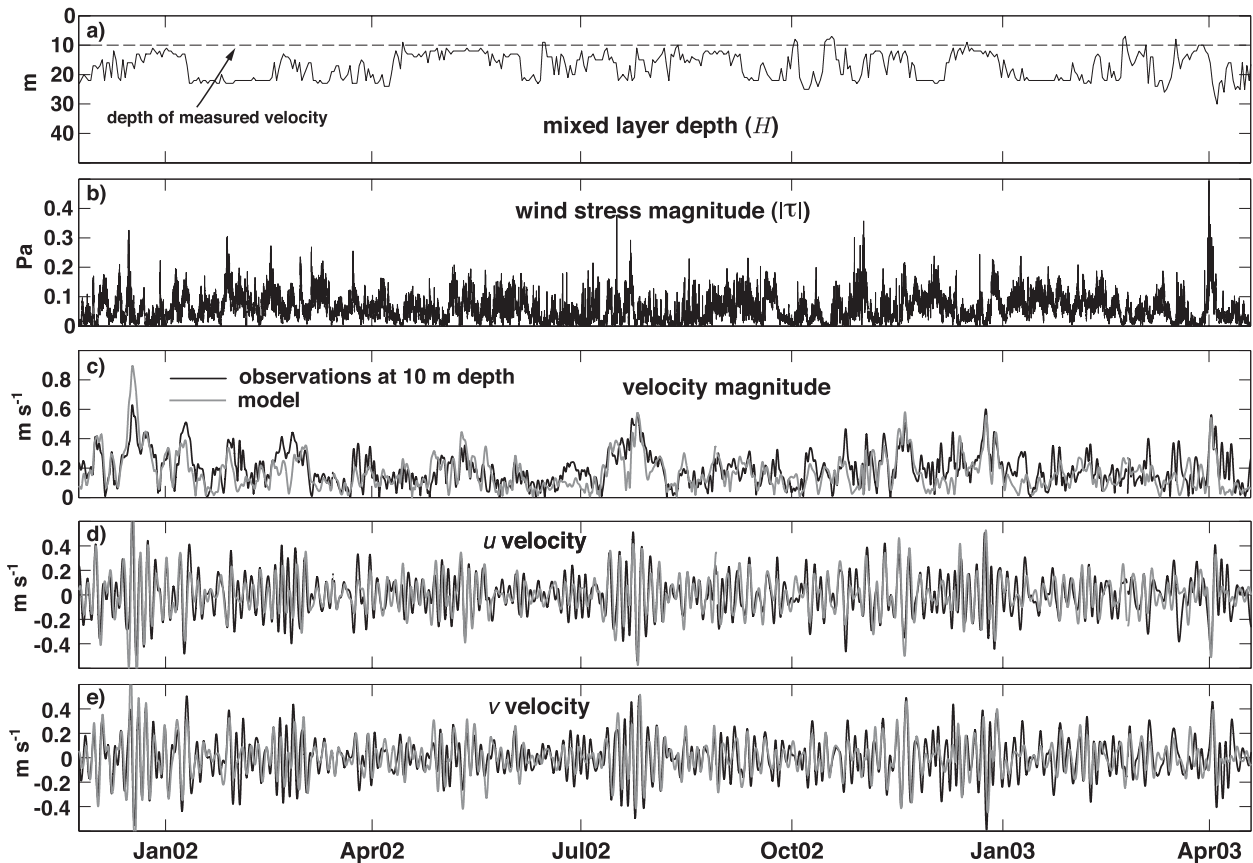


FIG. 5. Details of a subset of PM70 model variables at 8°N with a comparison to observed velocity: (a) mixed layer depth estimated from temperature data; (b) 4-h boxcar-averaged wind stress magnitude; (c) comparison of observed (black) and model (gray) velocity magnitude, with velocity measurements made at a depth of 10 m; and (d),(e) comparison of observed (black) and modeled (gray) velocity components.

where wind rotation has no effect on IKE flux. Although this test does not explicitly isolate the influence of CW forcing at f , the model IKE flux response function (Fig. 4) suggests that forcing with these characteristics will dominate the resonant response. As will be shown, an investigation of several strong individual resonant events clearly shows that resonance is due to wind stress rotating CW with a near-inertial period. Finally, it is also important to note that this approach does not capture resonant forcing from impulselike (duration $\leq 1/f$) wind stress events that occur in roughly the same direction and about an inertial period apart. Excluding this potential resonance may result in an underestimate of the degree of resonant forcing.

3) MODEL VALIDATION

A subsample of model input (H and τ) and output (u , v) at 8°N is shown in Fig. 5 along with a comparison to observed velocities at a depth of 10 m. With the mixed layer particularly well defined in this region (e.g., Wijesekera et al. 2005; J. B. Mickett and M. C. Gregg 2008, un-

published manuscript) and H almost always greater than 10 m for all locations (Fig. 5a), mixed layer velocities are likely predominantly slablike and are well represented by the single-point current measurements. Because forced inertial motions contain frequencies outside of the inertial band, for consistency both the model and observed velocities have been bandpassed with a third-order Butterworth filter from $0.5f$ to $2\pi/[26 \text{ h}]$ prior to comparison. Consistent with previous findings (e.g., Pollard 1980; Paduan et al. 1989; Firing et al. 1997; PF06), the model shows considerable skill with $R^2 = 0.45\text{--}0.5$ for both u and v velocities at all locations when compared with buoy velocity data.

Model Π_w is validated by a comparison to IKE flux calculated using the observed mixed layer currents when available (Fig. 6). As found here and as noted by others (e.g., D'Asaro 1985; Alford 2001; Watanabe and Hibiya 2002), Π_w is relatively insensitive to the value of r used but somewhat sensitive to H , because Z_I is inversely proportional to H . Consistent with the findings of PF06, this comparison shows that the model flux typically

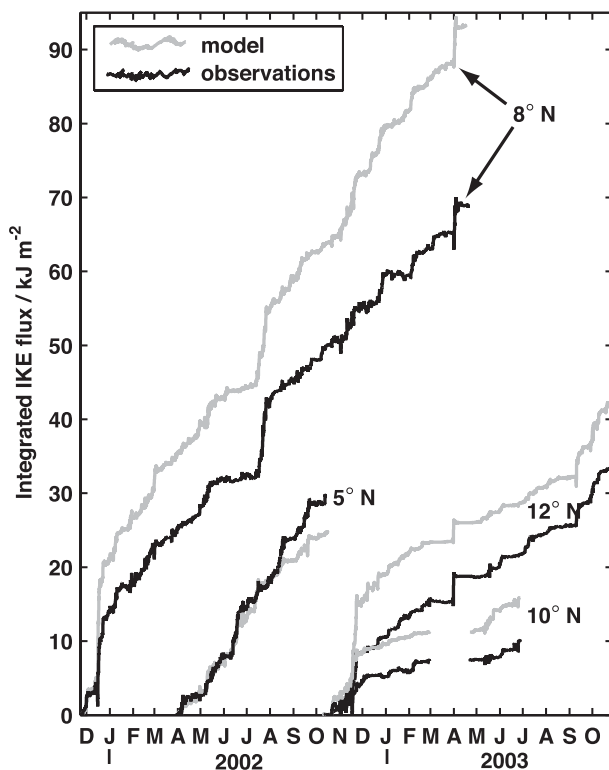


FIG. 6. Comparison of model (gray) and observationally based estimate (black) values of time-integrated IKE flux ($\int \Pi_w dt$, or inertial wind work) at each buoy. The span of integration is limited to times of continuous mixed layer current meter observations.

overestimates Π_w . However, here the PM70 model performs considerably better than in PF06, with model time-integrated fluxes on average only about 30%–60% greater than estimates based on observations, compared with roughly 25%–400% in PF06. The improved model performance may be partly due to the particularly well-defined mixed layer and exceptionally strong stratification below the mixed layer in the northeast tropical Pacific (Wijesekera et al. 2005; J. B. Mickett and M. C. Gregg 2008, unpublished manuscript), which could result in more slablike mixed layer velocities and may support large increases in mixed layer KE from wind forcing. Additionally, choosing a definition of the mixed layer depth that is coincident with the top of the seasonal thermocline (which may include weak stratification that does not act as a significant barrier to vertical momentum fluxes)—versus a definition of H that may exclude regions of relatively weak stratification—may be more appropriate given the assumptions of the PM70 model. Finally, the difference may also be due to differences in the predominant dynamics, with mixed layer velocities along 95°W dominated by local wind stress forcing and sites discussed in PF06 (including 10°N, 125°W) more heavily influenced by remote processes. Consistent with

PF06, the largest discrepancies between the model and observationally based estimates occur early during strong forcing events. Despite differences between model and observationally based fluxes, because the model somewhat consistently overestimates the fluxes and does exceptionally well at getting the trend of integrated Π_w , it is an adequate tool to use for this study.

3. Observations and slab model results

a. Spectral characteristics of the observed wind stress

Rotary spectra (Gonella 1972) are used to investigate the frequency characteristics of the clockwise and counterclockwise components of wind stress, keeping in mind that, in addition to forcing near the natural frequency, resonance also depends upon the specific phase angle between the forcing τ and response τ_f . However, as previously discussed in section 2b, because wind stress forcing modifies the direction of mixed layer currents, decreasing the phase angle offset and increasing coherence between τ and \mathbf{u}_f , dominance of CW over CCW variance of wind stress near f in the rotary spectra is alone a good indicator of the potential for resonance to exist.

Spectral estimates are calculated using 10-min wind stress and Welch's method (Welch 1967), with half-overlapping, 28-day Hamming windows. To increase the sample size, and thus the frequency resolution, gaps in the wind time series were padded with zeros. Comparisons to spectral estimates computed over continuous data segments showed that this approach has an insignificant influence on spectral levels in the frequency range of interest, in particular the relative magnitudes of the rotary components. The seasonal variability of the forcing is investigated by separating data into 6-month periods spanning July–December and January–June. This specific choice for the seasonal division maximizes the difference between the rotary components over the frequency range of easterly waves at 10° and 12°N and is consistent with studies investigating the seasonal cycle of PEWs showing greatest activity from June to November (Roundy and Frank 2004; Serra et al. 2008).

Rotary spectra computed using all data (with data from different times of the year equally weighted; Figs. 7c,f,i,l) indicate that, for all locations except for 5°N, CW energy is roughly 1.5–5 times CCW energy over an exceptionally broad range of frequencies from near 1×10^{-4} Hz (2.7-h period) to about 1.6×10^{-6} Hz, or a period of about 7 days. At 5°N, the energy levels of the two rotary components are much more similar over this broad frequency range, with CCW energy slightly greater than CW energy (~ 1.1 – 1.2 times) at PEW and near-inertial frequencies.

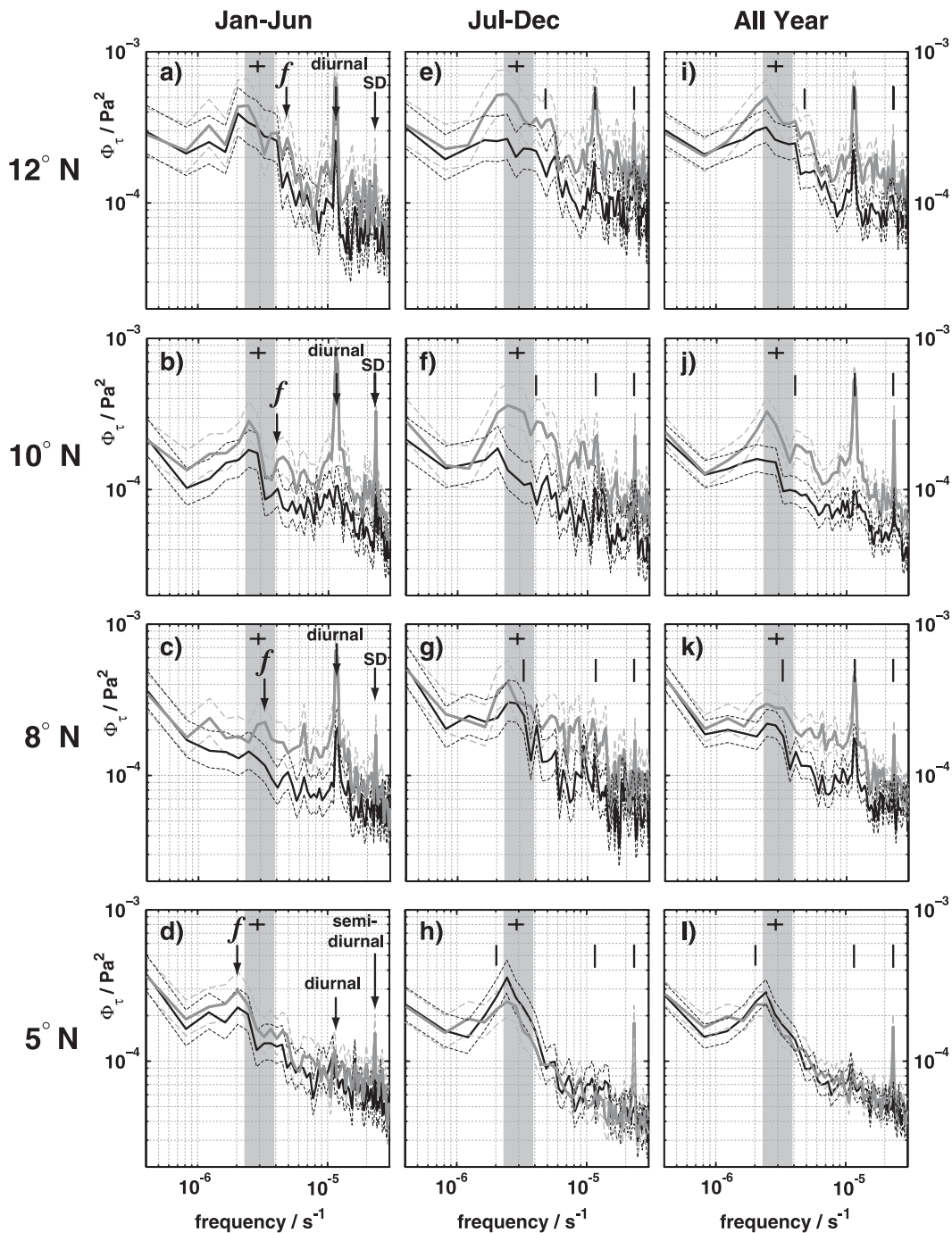


FIG. 7. Variance-preserving rotary spectra of 10-min wind stress from the TAO/EPIC moorings along 95°W at 12°, 10°, 8°, and 5°N, showing CW (gray) and CCW (black) components of the forcing. The 95% confidence limits are shown as dashed lines, and the frequency resolution at a period of 4 days is also shown (black cross). Spectra are shown for data from January to June, from July to December, and for all months. Gray shading shows the frequency band of PEWs (3–5 days), and vertical back lines show the local Coriolis (f), diurnal, and semidiurnal frequencies. Spectra are computed using Welch’s method with 50% overlapping Hamming windows of roughly a month of observations each. Data are from June 1999 to December 2003 (with gaps).

The spectral estimates show a broad peak spanning the expected period of easterly waves, or 3–5 days (Fig. 7), that is apparent in both rotary components for most locations and in both seasonal divisions. This peak is almost always toward the lower end of the PEW frequency range, is typically stronger in summer and fall months than in spring and winter, and in all cases—except for 5°N in the summer and fall—has more energy in the CW rotary component. It is noteworthy that the peak is largely absent in the CCW component at 10° and 12°N during summer–fall and at 8°N during winter/spring. At both 12° and 10°N, there also appears to be elevated wind stress variance in the CW component at a period near 2.5 days (4.5×10^{-6} Hz), which more closely overlaps with the local inertial period at these latitudes.

Seasonal rotary spectra show that at 12° and 10°N there is about 1.5–4 times more variance in the CW rotary component than the CCW component for data from July to December at PEW and near-inertial frequencies, with differences significant at the 95% level. This difference in the rotary components also exists at 8°N but is less with the CW component about 1.2–1.5 times the CCW component. At 5°N, the reverse is true, or the CCW component is about 1.2–1.4 times the CW component over this frequency range for the July–December period. In winter and spring (January–June), CW energy exceeds CCW energy at all latitudes over PEW and near-inertial frequencies, but the difference between components is less with CW energy on average about 1.5–2 times CCW energy.

It is worth noting that robust peaks at diurnal and semidiurnal (SD) frequencies are also present. Consistent with the findings of Ueyama and Deser (2008), the diurnal signal is weak or absent from the 5°N measurements. When present, both the diurnal and semidiurnal peaks at all locations have greater CW than CCW stress variance (5 times at 10°N). Additionally, the diurnal peak is consistently stronger in the winter and spring (January–May) than in the summer and fall (July–December). Also consistent with Ueyama and Deser (2008), the amplitude of the semidiurnal tidal peak at 5°N is roughly the same for both seasonal divisions.

b. Slab model results

1) THE SEASONAL AND INTERANNUAL VARIABILITY OF RESONANT FORCING

Consistent with the spectral characteristics of the forcing, model results show that at all locations except at 5°N forcing the PM70 model with the observed winds almost always results in equal or greater monthly averaged IKE flux ($\langle \Pi_w \rangle$, where the angle brackets denote monthly averages) than monthly mean IKE flux for model simulations using reversed-rotation winds ($\langle \Pi_{wr} \rangle$)

(Figs. 8a–d), strongly suggesting resonant forcing at these locations. At 10° and 12°N, the largest differences between $\langle \Pi_w \rangle$ and $\langle \Pi_{wr} \rangle$ occur in the summer and fall, suggesting that resonant wind forcing is strongest during this period at these latitudes. Time-integrated monthly averaged values of the fraction of IKE flux resulting from resonance $\int \langle \Pi_{w\phi} \rangle dt$ or “resonant wind work” manifests this seasonal cycle as milder slopes from January to about May and larger slopes from June to December (Figs. 8e–h). At 8°N, $\langle \Pi_w \rangle$ is about 1–2 mW m^{-2} (1.2–3.6 times) greater than $\langle \Pi_{wr} \rangle$ for December–July and roughly equal to $\langle \Pi_{wr} \rangle$ for the late summer and fall. During this latter period, however, there are only model results from one year (2002) for each of September and October, reducing confidence in the regularity of this pattern. Thus, model results suggest a seasonal cycle characterized by the strongest resonance in midsummer (July and August) and again in late fall/winter (December and January) and weak resonance or potential dissonance in September through November. At 5°N, reverse-rotation winds result in greater IKE flux ($\langle \Pi_{wr} \rangle > \langle \Pi_w \rangle$), except for December through March, when $\langle \Pi_w \rangle$ is as much as twice $\langle \Pi_{wr} \rangle$. Summing monthly averaged values of the fraction of IKE flux resulting from resonance $\langle \Pi_{w\phi} \rangle$ over a year shows that, at 8°, 10°, and 12°N, resonant forcing associated with observed winds on average results in about 10–15 kJ m^{-2} (15%–25%) more energy input over a year than nonresonant or neutral forcing conditions (Figs. 8e–h, Table 2). At 5°N annually integrated wind forcing is relatively neutral with resonant conditions in the winter and dissonant conditions present throughout the rest of the year.

Both the minimum and maximum ranges estimated by integrating the minimum and maximum monthly differences from all years (dashed lines in Fig. 8) and ranges in the net annual fluxes (Table 2) suggest the potential for large interannual variability in the degree of resonant forcing. Although for 10°N model results show a greater percentage of resonant forcing for years with the highest total cumulative IKE flux, suggesting that variability of resonant forcing causes much of the interannual variability, this is not the case at the other locations. At 5°N, for example, the largest percent of resonance (and largest $\Pi_{w\phi}$) occurs when the net annual IKE flux is the lowest of 5 yr.

2) AN EXAMINATION OF SELECT PEW RESONANT FORCING EVENTS

Focusing on several periods of strong resonant forcing by PEWs reveals important details about the nature of the resonance. One such period took place at 10°N from 22 to 28 July 2000 (Figs. 9a,b). Prior to, during, and following this event, wind rotation was predominantly CW

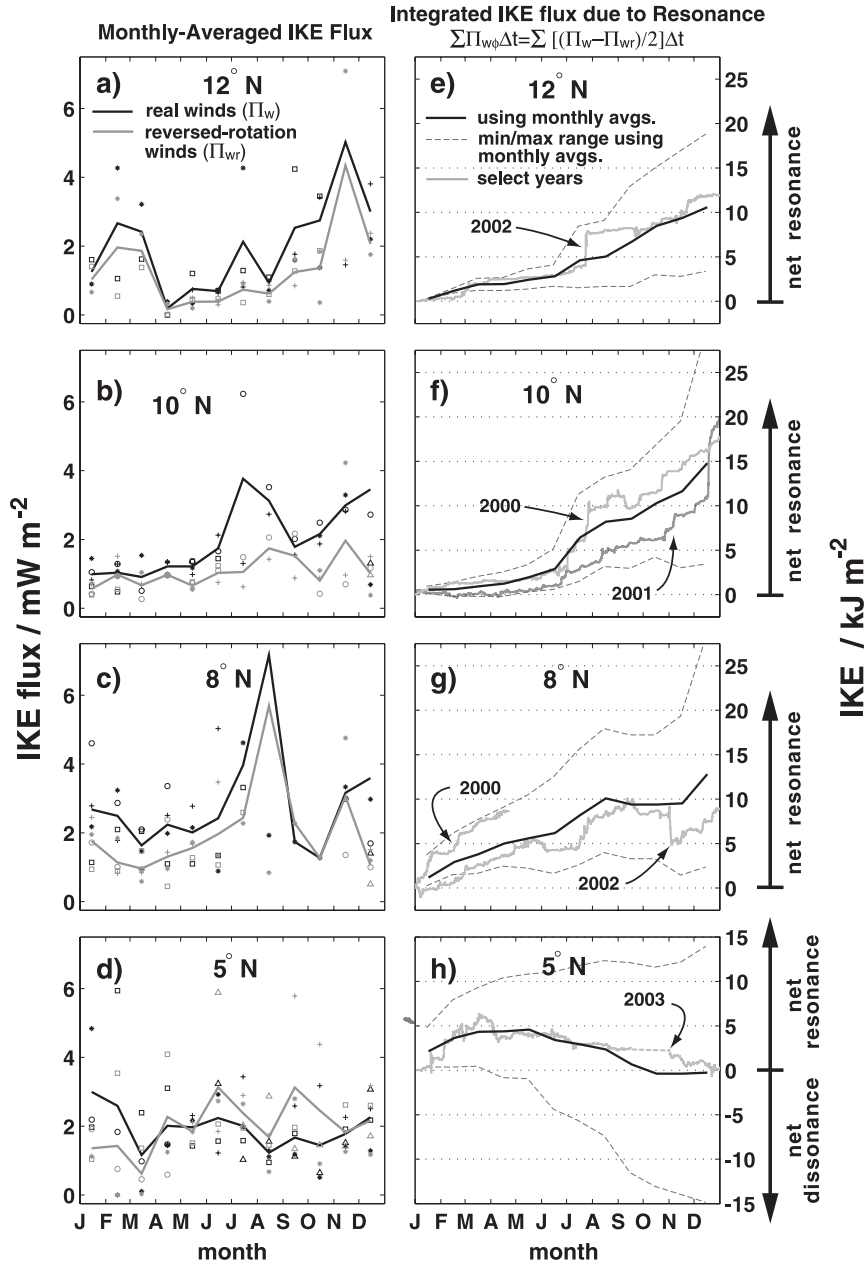


FIG. 8. (a)–(d), Monthly averages of model Π_w (black) and Π_{wr} (gray). Solid lines show the means of all monthly averages and markers show averages from individual years (with some off scale and not shown): triangle = 1999, circle = 2000, cross = 2001, asterisk = 2002, and open squares = 2003. (e)–(h) Time integration of $\Pi_{w\phi}$, with average monthly means (black) as well as select years (gray) plotted. A gap in model output for 2003 at 5°N (because of wind data gaps) is replaced with the mean slope over the gap period using all data (dashed). Thin dashed lines give the minimum/maximum ranges of the monthly mean integrated $\Pi_{w\phi}$.

at a period of about 3–5 days, consistent with westward propagation of PEWs with the zonal axis of the waves to the south. Indicating particularly well-developed PEWs during this timeframe, a PEW trough developed into what became Tropical Storm Emilia about 1400 km to the northwest (roughly 15°N, 107°W) on 27 July (in-

formation available online at <http://www.nhc.noaa.gov/2000emilia.html>). Time series of both time-integrated Π_w and Π_{wr} show that over a period of more than a week leading up to the event forcing was neutral with little IKE flux to the mixed layer. Although at times wind stress was significant during this period (>0.05 Pa),

TABLE 2. Model annually integrated IKE fluxes, where the angle brackets denote monthly averages. Months with <10 days of data are excluded from the average. Values outside of the parentheses show mean values for all years, and those in parentheses show minimum and maximum values from individual years. To address data gaps, minimum and maximum values are computed using the average of the monthly averaged data for a particular year. Only years with ≥ 6 months of data are used for minimum and maximum values, with at least 4 yr of data for each location. The percentage of Π_w due to resonance is given by $[\Pi_{w\phi}/\Pi_w] \times 100$.

Location	$\int \langle \Pi_w \rangle dt$ (kJ m ⁻²)	$\int \langle \Pi_{wr} \rangle dt$ (kJ m ⁻²)	Percent of $\int \langle \Pi_w \rangle dt$ due to resonance
12°N, 95°W	63.0 (50.6, 74.0)	41.9 (26.0, 50.3)	16.8% (16.0, 24.3)
10°N, 95°W	63.2 (49.2, 69.1)	33.6 (30.0, 38.4)	23.4% (11.0, 28.3)
8°N, 95°W	89.0 (72.0, 107.1)	63.4 (43.6, 74.8)	14.4% (10.8, 26.1)
5°N, 95°W	60.5 (49.2, 73.1)	61.1 (42.6, 92.3)	-0.4% (-18.5, 6.7)

because the direction of wind stress was often significantly different than that of the mixed layer currents, there was little addition of IKE to the mixed layer. The lack of coherence between τ and \mathbf{u}_l at this time appears to be related to a dominant period of wind stress rotation (and by inference PEWs) of roughly 5 days, whereas the inertial period is about 3 days (69 h). Large deviation from purely inertial mixed layer motions during this period suggests the forcing acted primarily to redirect currents, contributing little to mixed layer IKE.

From 22 to 28 July, however, the dominant period of wind rotation decreased to about 3 days and the wind stress became aligned with the inertial velocity: conditions favorable for resonance. Time-integrated Π_w over this period shows a net input of about 10 kJ m⁻², whereas integrated Π_{wr} only increases by about 2 kJ m⁻², indicating that resonance was exceptionally strong (Fig. 9b). This single event accounted for about one-third of the total resonant forcing and 15% of the total integrated IKE flux for that year. This finding, along with the plots of integrated $\Pi_{w\phi}$ for individual years (Figs. 8e–h), indicates that single events play a disproportionately large role in both annually integrated Π_w and $\Pi_{w\phi}$. Thus, forcing events with the largest wind stress–driven IKE fluxes to the ocean are also typically resonant. Although it has previously been shown that just a handful of forcing events can contribute to much of the annually integrated Π_w (e.g., D’Asaro 1985; Alford 2001; PF06), these results specifically show that within the northeast tropical Pacific these events are also typically strongly resonant, highlighting the importance of resonance to the energy transfer from the atmosphere to the ocean.

Another period of strong resonant forcing extending from mid-July to early August 2002 at 8°N again shows the tendency toward and importance of phase coherence of τ and \mathbf{u}_l (Figs. 9c,d). As for the case study at 10°N, the winds were predominantly CW at PEW frequencies during this time, with less consistency than during the 10°N case study period. As for the 10°N case study, resonance was associated with the intensification of two PEWs into two different hurricanes during this period: Douglas on 20 July, roughly 1300 km to the northwest, and Elida on 23 July,

about 500 km to the northwest (information available online at <http://www.nhc.noaa.gov/2002douglas.shtml> and <http://www.nhc.noaa.gov/2002elida.shtml>). Although there are times when the wind stress direction is significantly out of phase with that of the inertial currents (e.g., 20 and 29 July), relative coherence at other times suggests that CW rotation of τ at near- f frequencies is acting to strongly modify the direction of \mathbf{u}_l . This conclusion is also supported by the significant departure of \mathbf{u}_l from the local inertial period (e.g., 10–16 July). Again, as with the case at 10°N, resonance is in general strongest when the phases of \mathbf{u}_l and τ are coherent in time and both have appreciable magnitudes (Fig. 9d).

4. Discussion and conclusions

Much of the seasonal and meridional variability apparent in both the wind stress rotary spectra at PEW frequencies and in the resonantly generated IKE flux $\Pi_{w\phi}$ can be explained by the structure and seasonality of PEWs discussed in section 1 and as illustrated in Fig. 2. Again, resonant forcing of inertial motions is expected to result from CW-rotating winds north of the largely zonal axis of the PEW track, and dissonant forcing of inertial motions is expected from CCW winds south of this axis. As the PEW axis migrates meridionally with the seasons, so will the regions of resonance and dissonance. When PEWs are at their most northerly position of 8°–10°N in midsummer to early fall (e.g., Roundy and Frank 2004; Serra et al. 2008), both the rotary spectra and the model show strong CW forcing and potential for resonance (Figs. 7e,f, 8a,b). As expected, to the south at 5°N during this period we find CCW rotation of wind stress is dominant (Fig. 7h) and there is the likelihood of dissonant forcing of inertial motions (Fig. 8d). Consistent with a southward-shifted PEW zonal axis in the boreal winter/spring that is centered around 4°–5°N at 95°W, CW rotation of wind stress is weaker at 8°, 10°, and 12°N and is stronger at 5°N (Figs. 7a–d). Also consistent with this pattern, model results show weaker resonant conditions at 10° and 12°N and relatively strong resonant conditions at 5°N. At 8°N we find resonant conditions in

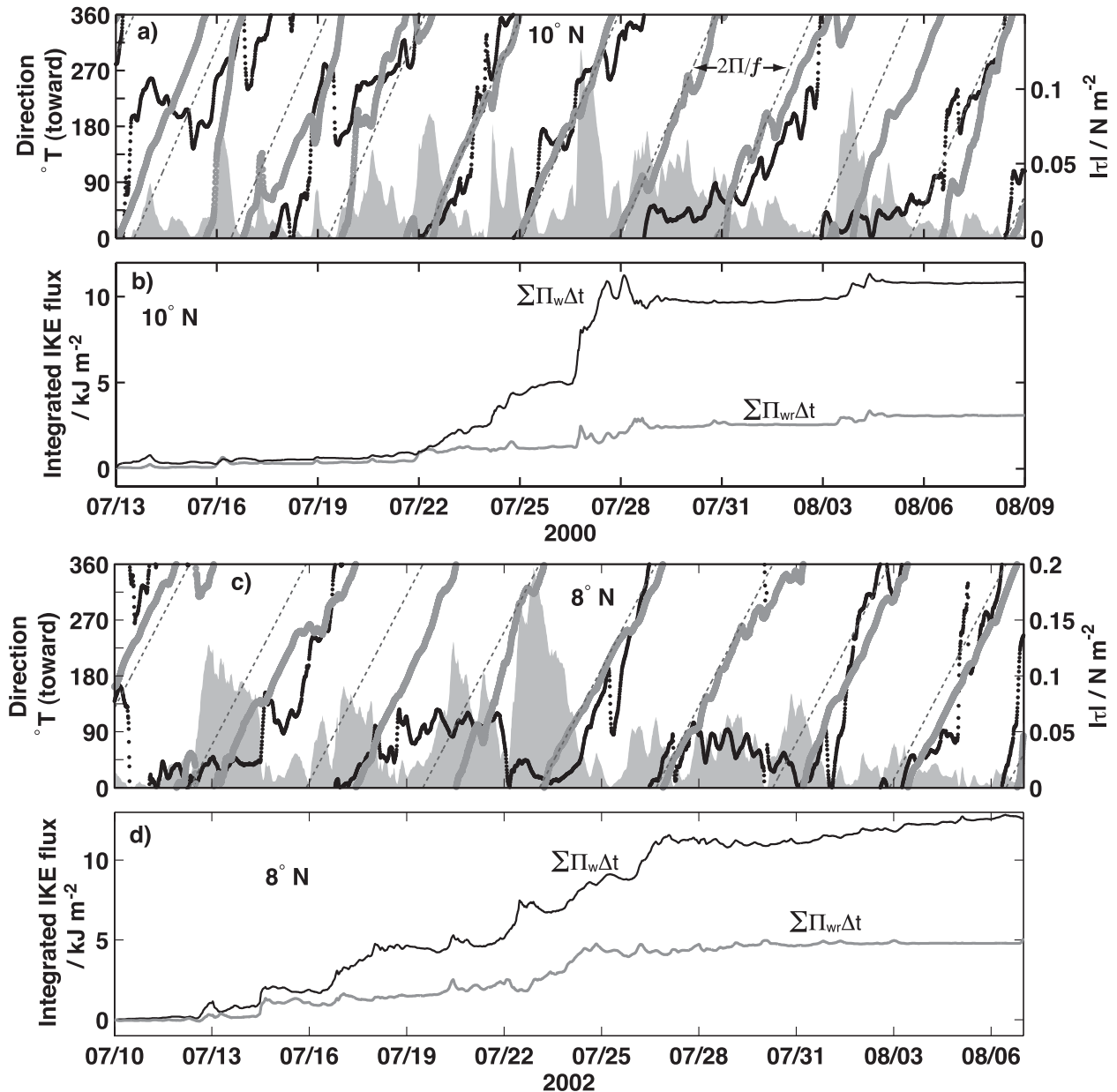


FIG. 9. Details of resonant forcing associated with PEWs during (a),(b) July–August 2000 at 10°N and (c),(d) July–August 2002 at 8°N : (a),(c) wind stress direction (black, left axis), magnitude (gray fill, right axis), and modeled inertial current direction (gray, left axis), where the phase change for local f is overplotted for reference (dashed gray), and (b),(d) time-integrated PM70 model IKE flux for real (black) and reversed-rotation (gray) winds.

all months except for September and October, when the PEWs are at their most northerly position.

The largest deviations from this expected pattern of resonant forcing occur in the late fall of 2001 at 8° , 10° , and 12°N when model simulations show strong resonant events even though the PEW track is expected to be considerably south of 8°N at this time. The timing of these events and the characteristics of the wind forcing suggest

that they could have been associated with another dominant mode of wind stress forcing in the region (viz., mountain gap wind outflow events). Driven by pressure gradients across Mexico and Central America associated with high pressure in the Gulf of Mexico, near-surface winds accelerate through gaps in the Sierra Madre, exiting to the Pacific near the Gulfs of Tehuantepec and Papagayo (Fig. 1). Gap wind outflow events are most common in the

late fall and winter when the ITCZ is at its most southerly position but have been observed to occur at other times (e.g., Roden 1961; McCreary et al. 1989; Steenburgh et al. 1998; Chelton et al. 2000; Xie et al. 2005). They can last from roughly 3–15 days and can extend up to 500 km from shore (e.g., McCreary et al. 1989; Xie et al. 2005) with their direct influence likely at all four study sites.

Specifically, one apparent gap wind resonant event took place in mid-December 2001 at both 8° and 10°N, with the PM70 model indicating that resonant wind forcing was responsible for roughly 10–15 kJ m⁻² of IKE input into the mixed layer over a 3-day period (Fig. 8f). Winds were relatively steady from the northeast before and after the event, suggesting that PEWs were not active at this time or were south of 8°N. During the event, the strongest winds were from the east to east-southeast at 10°N and from the east at 8°N, suggesting that they were associated with the Papagayo gap winds. Quick Scatterometer (QuikSCAT) satellite wind stress measurements support this interpretation, indicating that at this time both the Tehuantepec and Papagayo gap winds were active, with the latter influencing wind stress at both the 8° and 10°N study sites. Even though this event was strongly resonant, because the forcing was short lived (~1 day), the specific phase (and thus timing) of the largest wind stresses was critical for resonance. This is not necessarily the case for PEW-forced resonance, with forcing often occurring over at least several PEW periods allowing sufficient time to significantly modify the phase of the inertial currents (e.g., Fig. 9).

If timing is typically important for gap winds to resonantly force inertial motions, then these events also have the potential to strongly retard preexisting inertial motions and, therefore, on average may have little resonant effect. This conclusion is supported by several strong dissonant forcing events seen in the PM70 model simulations during the fall of 2002 at 10° and 8°N (Fig. 8g) and the absence of strong fall resonant events in years other than 2001. Additionally, in a study modeling the regional ocean circulation in response to the gap wind outflow events, McCreary et al. (1989) argues that because the gaps winds vary slowly with respect to the inertial period, they will only generate weak inertial motions. Thus, although we have not explicitly linked PEWs to the bulk of the estimated resonant forcing, the previous conclusion, in addition to the observed dominance of stress variance at PEW frequencies (e.g., Fig. 7), the strong sensitivity of Π_w to rotation at these frequencies, and consistency with the expected seasonality of PEWs all suggest that over the study period PEWs were responsible for most of the resonance indicated by PM70 model simulations. Significant interannual variability in net annual wind work

(i.e., Table 2) may be related to the inconsistency of gap wind resonant forcing, or as suggested by the findings of Gruber (1972) may be due to interannual variability in the meridional position of the ITCZ (and by inference of PEWs).

Accounting for potential overestimates of PM70 model Π_w by 30%–60% as found from comparisons with observationally based estimates (e.g., Fig. 6), results indicate that resonant forcing increases the net time-integrated flux of wind-driven IKE to the mixed layer, or wind work, at the 12°, 10°, and 8°N locations by roughly 5–15 kJ m⁻² (10%–25%) annually, or equivalently, on average resonance elevates Π_w by about 0.15–0.5 mW m⁻². With outward-radiating near-inertial internal waves responsible for a large fraction of the energy lost from mixed layer inertial motions (e.g., D'Asaro et al. 1995; Crawford and Large 1996), much of this added energy from resonance may eventually lead to elevated thermocline and abyssal mixing through the intermediary of internal waves. Additionally, although this study is limited to 95°W, observations suggesting that PEWs dominate synoptic low-level winds in the central and western Pacific (e.g., Reed and Recker 1971; Lau and Lau 1990; Roundy and Frank 2004; Serra et al. 2008) as well as the Atlantic (e.g., Thompson et al. 1979; Diedhiou et al. 2001; Kiladis et al. 2006) suggest that these findings may apply over a wide longitudinal range and may be important to the net input of IKE to the mixed layer within the tropics. A rough estimate of this importance can be obtained by integrating over the expected latitudinal range of this resonance or about 7°–12°N and over the zonal extent of the Pacific and Atlantic along these latitudes (about 180°) giving 5 GW. Also accounting for potential overestimates of 30%–60% for the IKE fluxes reported in Watanabe and Hibiya (2002) and Alford (2003) (observations by PF06 suggest could actually be a factor of 2 too high at 10°N, 125°W), a somewhat conservative estimate suggests that resonant forcing could contribute to as much as 30% of the total flux from the wind to inertial motions in the northern tropics. Finally, the strong air–sea coupling within the tropics largely driven through SST (Lindzen and Nigam 1987; Wallace et al. 1998; Chelton et al. 2001; Xie et al. 2005) and evidence showing that resonant forcing likely leads to increased turbulent entrainment and large, entrainment-driven SST changes (e.g., Crawford and Large 1996; Skillingstad et al. 2000) suggest that resonance could feed back onto atmospheric forcing. Investigating these potential connections may be a fruitful path for future research in this region.

Acknowledgments. ECMWF ERA-interim data used in this study have generously been provided by ECMWF.

This research was supported by the NOAA Climate Prediction Program for the Americas. The authors also wish to thank the two anonymous reviewers, whose comments helped to clarify and strengthen the manuscript.

REFERENCES

- Alford, M. H., 2001: Internal swell generation: The spatial distribution of energy flux from the wind to mixed-layer near-inertial motions. *J. Phys. Oceanogr.*, **31**, 2359–2368.
- , 2003: Improved global maps and 54-year history of wind-work on ocean inertial motions. *Geophys. Res. Lett.*, **30**, 1424, doi:10.1029/2002GL016614.
- Avila, L. A., 1991: Atlantic tropical systems of 1990. *Mon. Wea. Rev.*, **119**, 2027–2033.
- , and J. L. Guiney, 1998: Eastern North Pacific hurricane season of 1998. *Mon. Wea. Rev.*, **128**, 2990–3000.
- Chang, C. P., 1970: Westward propagating cloud patterns in the tropical Pacific as seen from time-composite satellite photographs. *J. Atmos. Sci.*, **27**, 133–138.
- Chelton, D. B., M. H. Freilich, and S. K. Esbensen, 2000: Satellite observations of the wind jets off Central America. Part I: Case studies and statistical characteristics. *Mon. Wea. Rev.*, **128**, 1993–2018.
- , and Coauthors, 2001: Observations of coupling between surface wind stress and sea surface temperature in the eastern tropical Pacific. *J. Climate*, **14**, 1479–1498.
- Crawford, G. B., 1993: Upper ocean response to storms—A resonant system. Ph.D. thesis, University of British Columbia, 277 pp.
- , and W. G. Large, 1996: A numerical investigation of resonant inertial response of the ocean to wind forcing. *J. Phys. Oceanogr.*, **26**, 873–891.
- Cronin, M. F., N. Bond, C. Fairall, J. Hare, M. J. McPhaden, and R. A. Weller, 2002: Enhanced oceanic and atmospheric monitoring underway in eastern Pacific. *Eos, Trans. Amer. Geophys. Union*, **83**, 210–211.
- , C. W. Fairall, and M. J. McPhaden, 2006: An assessment of buoy-derived and numerical weather prediction surface heat fluxes in the tropical Pacific. *J. Geophys. Res.*, **111**, C06038, doi:10.1029/2005JC003324.
- D'Asaro, E. A., 1985: The energy flux from the wind to near-inertial motions in the surface layer. *J. Phys. Oceanogr.*, **15**, 1043–1059.
- , C. C. Eriksen, M. D. Levine, P. Niiler, C. A. Paulson, and P. Van Meurs, 1995: Upper-ocean inertial currents forced by a strong storm. Part I: Data and comparisons with linear theory. *J. Phys. Oceanogr.*, **25**, 2909–2936.
- Diedhiou, A., S. Janicot, A. Viltard, and P. de Félice, 2001: Composite patterns of easterly disturbances over West Africa and the tropical Atlantic: A climatology from the 1979–95 NCEP/NCAR reanalyses. *Climate Dyn.*, **18**, 241–253.
- Firing, E., R.-C. Lien, and P. Müller, 1997: Observations of strong inertial oscillations after the passage of Tropical Cyclone Ofa. *J. Geophys. Res.*, **102** (C2), 3317–3322.
- Gonella, J., 1972: A rotary-component method for analysing meteorological and oceanographic vector time series. *Deep-Sea Res.*, **19**, 833–846.
- Gruber, A., 1972: Fluctuations in the position of the ITCZ in the Atlantic and Pacific Oceans. *J. Atmos. Sci.*, **29**, 193–197.
- Gu, G., and C. Zhang, 2002: Westward-propagating synoptic-scale disturbances and the ITCZ. *J. Atmos. Sci.*, **59**, 1062–1075.
- Kiladis, G., C. D. Thorncroft, and N. M. J. Hall, 2006: Three-dimensional structure and dynamics of African easterly waves. Part I: Observations. *J. Atmos. Sci.*, **63**, 2212–2230.
- Large, W. G., and S. Pond, 1981: Open ocean momentum flux measurements in moderate to strong winds. *J. Phys. Oceanogr.*, **11**, 324–336.
- , and G. B. Crawford, 1995: Observations and simulations of upper-ocean response to wind events during the ocean storms experiment. *J. Phys. Oceanogr.*, **25**, 2831–2852.
- , J. C. McWilliams, and S. C. Doney, 1994: Oceanic vertical mixing: A review and a model with a nonlocal boundary layer parameterization. *Rev. Geophys.*, **32**, 363–403.
- Lau, K.-H., and N. C. Lau, 1990: Observed structure and propagation characteristics of tropical summertime synoptic scale disturbances. *Mon. Wea. Rev.*, **118**, 1888–1913.
- Lindzen, R. S., and S. Nigam, 1987: On the role of sea-surface temperature-gradients in forcing low-level winds and convergence in the tropics. *J. Atmos. Sci.*, **44**, 2418–2436.
- McCreary, J. P., H. S. Lee, and D. B. Enfield, 1989: The response of the coastal ocean to strong off shore winds: With application to circulations in the Gulfs of Tehuantepec and Papagayo. *J. Mar. Res.*, **47**, 81–109.
- Mitchell, T. P., and J. M. Wallace, 1992: The annual cycle in equatorial convection and sea surface temperature. *J. Climate*, **5**, 1140–1156.
- Nitta, T., Y. Nakagomi, Y. Suzuki, N. Hasegawa, and A. Kadokura, 1985: Global analysis of the lower-tropospheric disturbances in the tropics during the northern summer of the FGGE year. Part I: Global features of the disturbances. *J. Meteor. Soc. Japan*, **63**, 1–19.
- Paduan, J. D., R. A. de Soerke, and R. A. Weller, 1989: Inertial oscillations in the upper ocean during the Mixed Layer Dynamics Experiment (MILDEX). *J. Geophys. Res.*, **94** (C4), 4835–4842.
- Petersen, W. A., R. Cifelli, D. J. Boccippio, S. A. Rutledge, and C. Fairall, 2003: Convection and easterly wave structures observed in the eastern Pacific warm pool during EPIC-2001. *J. Atmos. Sci.*, **60**, 1754–1772.
- Plueddemann, A. J., and J. T. Farrar, 2006: Observations and models of the energy flux from the wind to mixed-layer inertial currents. *Deep-Sea Res. II*, **53**, 5–30.
- Pollard, R. T., 1980: Properties of near-surface inertial oscillations. *J. Phys. Oceanogr.*, **10**, 385–398.
- , and R. C. Millard, 1970: Comparison between observed and simulated wind-generated inertial oscillations. *Deep-Sea Res.*, **17**, 153–175.
- Price, J. F., R. A. Weller, and R. Pinkel, 1986: Diurnal cycling: Observations and models of the upper ocean response to diurnal heating, cooling, and wind mixing. *J. Geophys. Res.*, **91** (C7), 8411–8427.
- Reed, R. J., and E. E. Recker, 1971: Structure and properties of synoptic-scale wave disturbances in the equatorial western Pacific. *J. Atmos. Sci.*, **28**, 1117–1133.
- Roden, G. J., 1961: On the wind-driven circulation in the Gulf of Tehuantepec and its effect upon surface temperatures. *Geophys. Int.*, **1**, 55–72.
- Roundy, P. E., and W. M. Frank, 2004: A climatology of waves in the equatorial region. *J. Atmos. Sci.*, **61**, 2105–2132.
- Serra, Y. L., and R. A. Houze, 2002: Observations of variability on synoptic timescales in the East Pacific ITCZ. *J. Atmos. Sci.*, **59**, 1723–1743.
- , G. Kiladis, and M. F. Cronin, 2008: Horizontal and vertical structure of easterly waves in the Pacific ITCZ. *J. Atmos. Sci.*, **65**, 1266–1284.

- Skyllingstad, E. D., W. D. Smyth, and G. B. Crawford, 2000: Resonant wind-driven mixing in the ocean boundary layer. *J. Phys. Oceanogr.*, **30**, 1866–1890.
- Steenburgh, W. J., D. M. Shultz, and B. A. Colle, 1998: The structure and evolution of gap outflow over the Gulf of Tehuantepec, Mexico. *Mon. Wea. Rev.*, **47**, 81–109.
- Tai, K.-S., and Y. Ogura, 1987: An observational study of easterly waves over the eastern Pacific in the northern summer using FGGE data. *J. Atmos. Sci.*, **44**, 339–361.
- Thompson, R. M., S. W. Payne, E. E. Recker, and R. J. Reed, 1979: Structure and properties of synoptic-scale wave disturbances in the intertropical convergence zone of the eastern Atlantic. *J. Atmos. Sci.*, **36**, 53–72.
- Ueyama, R., and C. Deser, 2008: A climatology of diurnal and semidiurnal surface wind variations over the tropical Pacific Ocean based on the Tropical Atmosphere Ocean moored buoy array. *J. Climate*, **21**, 593–607.
- Wallace, J. M., E. M. Rasmusson, T. P. Mitchell, V. E. Kousky, E. S. Sarachik, and H. von Storch, 1998: On the structure and evolution of ENSO-related climate variability in the tropical Pacific: Lessons from TOGA. *J. Geophys. Res.*, **103**, 14 241–14 259.
- Wang, C.-C., and G. Magnusdottir, 2006: The ITCZ in the central and eastern Pacific on synoptic time scales. *Mon. Wea. Rev.*, **134**, 1405–1421.
- Watanabe, M., and T. Hibiya, 2002: Global estimates of the wind-induced energy flux to inertial motions in the surface mixed layer. *Geophys. Res. Lett.*, **29**, 1239, doi:10.1029/2001GL014422.
- Welch, P. D., 1967: The use of fast Fourier transform for the estimation of power spectra: A method based on time averaging over short, modified periodograms. *IEEE Trans. Audio Electroacoust.*, **15**, 70–73.
- Wheeler, M., and G. Kiladis, 1999: Convectively coupled equatorial waves: Analysis of clouds and temperature in the wavenumber–frequency domain. *J. Atmos. Sci.*, **56**, 374–399.
- Wijesekera, H. W., D. L. Rudnick, C. A. Paulson, S. D. Pierce, W. S. Pegau, J. Mickett, and M. C. Gregg, 2005: Upper ocean heat and freshwater budgets in the eastern Pacific warm pool. *J. Geophys. Res.*, **110**, C08004, doi:10.1029/2004JC002511.
- Xie, S.-P., H. Xu, W. S. Kessler, and M. Nonaka, 2005: Air–sea interaction over the eastern Pacific warm pool: Gap winds, thermocline dome, and atmospheric convection. *J. Climate*, **18**, 5–20.